Meccanica (2016) 51:3025–3042
DOI 10.1007/s11012-016-0558-0

50TH ANNIVERSARY OF MECCANICA

Convergence of numerical simulations of turbulent wall-bounded flows and mean cross-flow structure of rectangular ducts

Ricardo Vinuesa · Cezary Prus · Philipp Schlatter · Hassan M. Nagib

Received: 16 August 2016 / Accepted: 17 October 2016 / Published online: 26 October 2016

Abstract Convergence criteria for direct numerical simulations of turbulent channel and duct flows are proposed. The convergence indicator for channels is defined as the deviation of the nondimensional total shear-stress profile with respect to a linear profile, whereas the one for the duct is based on a nondimensional streamwise momentum balance at the duct centerplane. We identify the starting (T_S) and averaging times (T_A) necessary to obtain sufficiently converged statistics, and also find that optimum convergence rates are achieved when the spacing in time between individual realizations is below $\Delta t^+ = 17$. The in-plane structure of the flow in turbulent ducts is also assessed by analyzing square ducts at $Re_{\tau,c} \simeq 180$ and 360 and rectangular ducts with aspect ratios 3 and 10 at $Re_{\tau,c} \simeq 180$. Identification of coherent vortices shows that near-wall streaks are located in all the duct cases at a wall-normal distance of $y^+ \simeq 40$ as in Pinelli et al. (J Fluid Mech 644:107–122, 2010). We also find that large-scale motions play a crucial role in the streamline pattern of the secondary flow, whereas near-wall structures highly influence the streamwise vorticity pattern. These conclusions extend the findings by Pinelli et al. to other kinds of large-scale motions in the flow through the consideration of wider ducts. They also highlight the complex and multiscale nature of the secondary flow of second kind in turbulent duct flows.

Keywords Wall-bounded turbulence · Direct numerical simulation · Convergence · Secondary flow · Turbulent structures

R. Vinuesa (✉) · C. Prus · P. Schlatter
Linné FLOW Centre, KTH Mechanics, Royal Institute of Technology, Stockholm, Sweden
e-mail: rvinuesa@mech.kth.se

H. M. Nagib
Department of Mechanical, Materials and Aerospace Engineering (MMAE), Illinois Institute of Technology (IIT), Chicago, IL 60616, USA
e-mail: nagib@iit.edu

1 Introduction

Numerical simulations have become, together with new experimental techniques, the key to understanding some of the most intriguing aspects of wall-bounded turbulence. Since the well-known work on channel flows by Kim et al. [1] in the late 1980s, the increase of computational power and the development of highly scalable numerical algorithms has allowed the computation of increasingly higher Reynolds numbers, as well as more complicated geometries. Some of the most relevant direct numerical simulations (DNSs) of wall-bounded turbulence are the channel flows computed by del Álamo et al. [2], Lozano-Durán and Jiménez [3] and Lee and Moser [4] (up to friction Reynolds numbers of $Re_\tau \simeq 2000$, $\simeq 4200$ and $\simeq 5200$ respectively), the ZPG boundary layers by Schlatter and Örlü [5] and Sillero et al. [6] (up to Re_τ values of $\simeq 1000$ and $\simeq 2000$ respectively),

as well as the pipe flows by Wu and Moin [7] and El Khoury et al. [8] (with a maximum Re_τ of $\simeq 1000$ in both cases). Note that the friction Reynolds number is defined in terms of the length scale h (which is the channel half-height, the pipe radius or the boundary-layer thickness) and the friction velocity $u_\tau = \sqrt{\tau_w/\rho}$ (where τ_w is the wall-shear stress and ρ is the fluid density). These numerical experiments have helped to understand the buffer sublayer, and now start to shed light on the dynamics of the log layer and the outer-layer structures.

Most experimental studies of wall-bounded turbulence provide detailed descriptions of the measurement techniques and the experimental setup employed during their research. For example, Österlund [9] elaborates on the design of the wind tunnel used in his work (the MTL wind tunnel at KTH), he provides extensive descriptions of the instrumentation he used (probe calibration, sampling time...) and he describes the different trip designs considered for tripping the flow under study. Despite the wealth of descriptions of experimental setups available in the literature, physical experiments are thoroughly scrutinized before they are employed to validate scaling laws or theories. As discussed by Nagib et al. [10] and Chauhan et al. [11], the tripping device employed to trigger transition to turbulence may play an important role in the development of a boundary layer, leading to underdeveloped flows if not done properly. This was also observed recently by Vinuesa et al. [12] after carefully assessing the inflow conditions of numerical simulations and comparing with experimental data. Other factors that highly influence experimental studies of wall-bounded turbulence are the necessity of adequate corrections to the probe measurements, discussed in detail in Ref. [13], or the relation between the probe size and the smallest turbulent scales, which may lead to a contamination of the near-wall measurements if the probe is not small enough [14]. The latter aspect has motivated the construction of the experimental facility CICLoPE at the University of Bologna (Italy), in which the size of the smallest turbulent scales is increased by developing a larger experimental facility [15]. The issue of the averaging time required to obtain converged turbulence statistics in turbulent-boundary-layer experiments was addressed by Klewicki and Falco [16]. In their study, they obtained cumulative estimates of statistics of a number of observables, including velocity and vorticity components, double products and time derivatives. They also assessed the necessary averaging times in different parts of the boundary layer, considering the effects of shear, intermittency and near-wall dynamics. They concluded that in order to obtain converged turbulence statistics up to the fourth moment it is necessary to average for at least 6000 convective time units (defined as the ratio of the boundary-layer thickness δ and the freestream velocity U_∞). Antonia et al. [17] provided a compilation of empirical relations to estimate the required averaging time for a particular level of convergence in turbulent jets. More recent experimental studies [18] have reported longer averaging periods of around 25,000 convective time units used to obtain converged turbulence statistics.

On the other hand, and as discussed by Schlatter and Örlü [5], the DNS data available in the literature are hardly scrutinized. Interestingly, these data show dispersions of up to 5 % in the shape factor $H = \delta^*/\theta$ (where δ^* and θ are the displacement and momentum thicknesses respectively), and up to 20 % in skin friction. Aspects which are barely mentioned in most numerical studies, such as the numerical mechanism used to trigger transition to turbulence, can produce important differences in the computed results. Schlatter and Örlü [19] analyzed the downstream evolution of several integral, mean and fluctuating properties of simulated ZPG turbulent boundary layers, and showed that different inflow conditions and tripping mechanisms explain most of the discrepancies between the various low-*Re* DNS databases. Another characteristic that is not described in detail in the literature and significantly influences the results of a numerical simulation is convergence. Most numerical studies devote, at most, one or two lines to explain how the convergence of their statistics was assessed. A notable exception is the work by Oliver et al. [20], where the authors address the problem of statistical convergence of DNS in a systematic way. The article points out that the traditional mesh size sensitivity study using Richardson extrapolation should not be performed for the DNS analyses of turbulent flows, because of the presence of sampling errors. This may result in the discretization error not decreasing exponentially with progressively finer mesh sizes. To overcome this obstacle the authors propose a new approach which takes into account the inaccuracies in

both sampling and discretization: the so-called Bayesian Richardson extrapolation. An auto-regressive model is then fitted to the obtained results in order to describe the sampling error (taking into account the autocorrelation of sampled data), which is then used to estimate the common influence of discretization and statistical errors. Other studies addressing the issue of statistical convergence in DNS data of turbulent channel flows are the work by Hoyas and Jiménez [21] and the recent work by Thompson et al. [22], in this case considering the momentum-balance equation. However, due to the lack of consensus in the community, we see the need of developing a systematic approach to assess convergence in order to minimize discrepancies between simulations, and ensure maximum accuracy of the results. One desirable feature of such a criterion would be a direct relation with the physics of the flow instead of using a purely statistical investigation. The characteristics of the convergence criterion proposed here are discussed in detail below.

Another aspect widely discussed in the area of turbulence research is the presence of coherent structures and their role in turbulent momentum transfer across different scales. For instance, del Álamo et al. [23] assessed the role of vortex clusters in wall-bounded turbulent flows, Lozano-Durán et al. [24] the impact of three-dimensional sweeps and ejections, and Lozano-Durán and Jiménez [3] tracked both types of structures in time and developed a new approach to the study of the dynamics of turbulent flows based on them. In the present study the λ_2 method developed by Jeong and Hussain [25] is used to identify vortex clusters in turbulent rectangular ducts of different aspect ratios, at $Re_{\tau,c} \simeq 180$ and 360 (note that $Re_{\tau,c}$ is defined in terms of the centerplane friction velocity $u_{\tau,c}$). A sequence of instantaneous velocity fields is used to obtain probability density functions of the locations of the vortex clusters, and their connection with the mean secondary flow is assessed in detail.

The present article is structured as follows: convergence criteria for channels and ducts are proposed and compared with other indicators available in the literature in Sect. 2; numerical simulations performed in the present study and convergence results for channels and ducts are presented in Sect. 3; in Sect. 4 several criteria for vortex identification are described and the cross-flow of turbulent ducts is characterized; and the conclusions of this study are summarized in Sect. 5.

2 Convergence in numerical simulations of wall-bounded turbulence

The first step to study convergence is the identification of initial transients, i.e., what is the time T_S when averaging should start. During the transient period, the flow has to evolve from the initial conditions (whether they are defined by a laminar field with superimposed disturbances, or a turbulent field extracted from a previous simulation) to a state which is representative of turbulence. This period is usually shorter if the initial conditions are already turbulent than if they are laminar. Even in the first case the flow needs some time to adjust from the initial field, so T_S will not be zero. In the second case, T_S depends on the kind of disturbance used to trigger transition to turbulence. For instance, a duct flow with aspect ratio 3 (where the aspect ratio AR is defined as the duct width W_d divided by its total height $2h$) and $Re_{\tau,c} \simeq 180$ will relaminarize if a laminar profile with superimposed high-frequency Gaussian noise is used as starting field. However, if a low-frequency tripping mechanism similar to the one described by Schlatter and Örlü [19] is used with the initial laminar profile, then the flow transitions to turbulence as discussed by Vinuesa et al. [26]. In any case, it is important to identify T_S properly, since the initial transient is not representative of the flow being simulated, and thus averaging times required for convergence may increase if included in the statistics.

After identifying and discarding the initial transients, we need to determine the averaging time T_A required to obtain sufficiently converged statistics. It is important to note the difference between T_S and T_A, and especially the relevance of T_S: longer averaging times T_A may be required to ensure proper convergence if the considered T_S is too small, i.e., if part of the initial transients are included in the statistics. All the instantaneous fields computed at times $t > T_S$ are physical (represent a turbulent field at a given instant), so in principle if these fields are averaged over sufficiently high values of T_A it will be possible to achieve convergence.

2.1 Literature review of convergence criteria

Existing convergence guidelines for turbulent channel and duct-flow DNSs are summarized in Tables 1 and 2, respectively. Note that in these tables U_b is the bulk velocity integrated over the cross-sectional area. We also classified those guidelines into two categories: criteria to indetify T_S and criteria to determine T_A. The initial transients are identified in all the channel cases by assessing whether the resulting total shear stress was linear or not. However, the only discussion about T_A, provided both by Moser et al. [27] and del Álamo [28], is somewhat incomplete. In the case of ducts, there is more variety of criteria for T_S and T_A, although there is not any criterion based on what the converged state of the flow should be from a physical perspective, rather than seeking stationary behavior of statistics.

2.2 Definition of converged state

We propose to define a "converged state" for the channel flow, and evaluate how far from this state (how converged) the statistics are for all the possible $(T_S,\ T_A)$ combinations in the time history. A reasonable definition of such a converged state can be established from a momentum balance in the streamwise direction:

$$\frac{1}{\rho}\frac{\partial P}{\partial x} = \nu\frac{\partial^2 U}{\partial y^2} - \frac{\partial \overline{uv}}{\partial y}, \tag{1}$$

where P is the pressure, ν is the kinematic viscosity of the fluid, x and y the streamwise and wall-normal coordinates, U the streamwise mean velocity and $\overline{uv}$ the Reynolds shear stress. To allow comparisons between simulations, Eq. (1) can be expressed in wall units (denoted by the superscript "+"), where the velocity scale is the friction velocity u_τ and the length scale is the viscous length $\ell^* = \nu/u_\tau$. Doing so, and integrating the RHS with respect to y^+, one realizes that the total shear stress $\tau_{xy}^+ = Re^{-1}\partial U^+/\partial y^+ - \overline{uv^+}$ has to be linear. It is important to note that this is a direct consequence of the momentum balance (1), valid only for fully-developed channel and pipe flows, and therefore not true for low aspect ratio duct flows as will be shown below. Then, the equation characterizing the converged state of the channel flow is:

$$\tau_{xy}^+ = Re^{-1}\frac{\partial U^+}{\partial y^+} - \overline{uv^+} = 1 - \eta, \tag{2}$$

where η is the wall-normal coordinate scaled by the channel half-height h (outer scaling). In the case of duct flows, the converged state can be established from a streamwise momentum balance at the duct centerplane:

$$-\frac{\partial P^+}{\partial x^+} + Re^{-1}\frac{\partial^2 U^+}{\partial y^{+2}} - \frac{\partial \overline{uv^+}}{\partial y^+} - V^+\frac{\partial U^+}{\partial y^+} + Re^{-1}\frac{\partial^2 U^+}{\partial z^{+2}} = 0, \tag{3}$$

where V is the mean wall-normal velocity and z the spanwise coordinate. If the aspect ratio is low the side walls impact the flow at the duct centerplane, and therefore the convective term $V^+\partial U^+/\partial y^+$ and the spanwise viscous diffusion $Re^{-1}\partial^2 U^+/\partial z^{+2}$ are not

Table 1 Summary of convergence guidelines available in the literature for channel flows

DNS database	Scheme	T_S criterion	T_A criterion
Kim et al. [1]	Spectral	Linear profile of total shear stress and quasi-periodic total kinetic energy	Not specified
Moser et al. [27]	Spectral	Linear profile of total shear stress and quasi-periodic total kinetic energy	Stationary behavior of statistics. From their experience: $T_A \geq 10L_x/U_b$
Iwamoto et al. [29]	Spectral	Linear profile of total shear stress, stationary behavior of mean velocity and second-order moments at some y_{ref}	Not specified
del Álamo [28]	Spectral	Linear profile of total shear stress and quasi-periodic total kinetic energy	Stationary behavior of statistics. From their experience: $T_A \geq 10L_x/U_b$
Tuerke [30]	Spectral	Linear profile of total shear stress and deviatoric Reynolds stress $\overline{vw} = 0$	Not specified

Table 2 Summary of convergence guidelines available in the literature for duct flows

DNS database	Scheme	T_S criterion	T_A criterion
Kim et al. [1]	Spectral	Linear profile of total shear stress and quasi-periodic total kinetic energy	Not specified
Gavrilakis [31]	2nd order finite-differences	Not specified (2 low-res. precursor runs)	Variation of $U_b < 0.2\,\%$ and of total kinetic energy $< 5\,\%$
Huser and Biringen [32]	4th order fin.-diff. and spectral	Linear profile of total shear stress and constant total kinetic energy	Not specified
Pinelli et al. [33] Uhlmann et al. [34]	Spectral	Not specified	$T_A > 2000h/U_b$, based on critical channel conditions [35]
Krasnov et al. [36]	2nd order finite-differences	Steady Re_τ and other integral quantities	Not specified

zero at the centerplane. This means that we cannot proceed with direct integration as in the channel, and therefore the total shear τ^+_{xy} is not linear. As a consequence, the converged state for a duct is defined through Eq. (3), and not through Eq. (2) which is only valid for spanwise-periodic channels (or possibly rectangular ducts of sufficiently high aspect ratio).

2.3 Convergence indicator and normalized eddy turnover time

After defining the converged state for channel and duct flows, we need to assess whether the available data are close to this state or not. To this end, we need to define a convergence indicator ε, which should asymptotically decay to zero as statistical convergence is approached. In the case of channels, $\varepsilon_{\text{channel}}$ will be the RMS norm of the deviation between the total shear stress and a linear profile, i.e., the LHS and the RHS of Eq. (2). On the other hand, $\varepsilon_{\text{duct}}$ will be evaluated as the residual of Eq. (3) based on RMS norm. The RMS norm is defined over the whole profile as follows:

$$||\cdot|| = \left[\frac{1}{h}\int_0^h (\cdot)^2 \, \mathrm{d}y\right]^{1/2}. \tag{4}$$

If wall-normal symmetry is not applied, then the integration will be carried out in the complete domain. In the next section we will use these criteria on three flow cases to determine the appropriate T_S and T_A values to achieve convergence. Here, let us consider available data in the literature, and determine the corresponding ε values to evaluate their convergence. In order to compare the different T_S and T_A values, we first consider the eddy turnover time $\mathrm{ETT} = tu_\tau/h$. Here, the characteristic period of the largest turbulent scales, h/u_τ, is used to normalize the time t. However, although this definition accounts for the differences in friction velocities among simulations, it does not take into account the different computational box sizes. We define the following "normalized eddy turnover times":

$$\mathrm{ETT}^*_{\text{channel}} = \mathrm{ETT}_{\text{channel}} \frac{L_x L_z}{L_{x,\min} L_{z,\min}}, \tag{5}$$

$$\mathrm{ETT}^*_{\text{duct}} = \mathrm{ETT}_{\text{duct}} \frac{L_x}{L_{x,\min}}, \tag{6}$$

where L_x, L_z are the streamwise and spanwise box lengths, and $L_{x,\min} = 6h, L_{z,\min} = 3h$ define the box size containing the minimal flow unit in the logarithmic layer, as discussed by Flores and Jiménez [37]. For ducts, only the ratio $L_x/L_{x,\min}$ is considered since x is the only homogeneous direction. With these definitions, we consider the fact that boxes with longer periodic dimensions effectively contain larger number of turbulent structures, and thus require shorter averaging times to reach the same level of convergence as a smaller box (as also observed by del Álamo [28]).

2.4 Summary of convergence results available in the literature

Tables 3 and 4 summarize convergence results from a wide range of DNS databases available in the literature. Note that the results presented in this section were obtained from the databases publicly available in

the websites from the various research groups, or based on data available in the corresponding publications. We calculated the averaging and starting times (when provided in the respective references) in ETT, and then applied the correction for box size proposed in Eqs. (5) and (6). In this sense, it is interesting to note that the same averaging period normalized in eddy turnover times can be very different in various cases after applying this correction. For instance, in Table 3, one can observe how the $Re_\tau = 396$ case from Iwamoto et al. [29] and the $Re_\tau = 2003$ channel from Hoyas and Jiménez [38] have similar averaging times when expressed in ETT* units: 176.8 and 135.5 respectively. However, when normalized in regular eddy turnover-time units, the lower *Re* case has an averaging period of more than 10 times the one with the larger *Re*. In addition, the second case exhibits a lower ε value, which means that it is more converged according to the already discussed criterion. The idea is that the higher *Re* case was computed in a larger box, which despite the fact of being more computationally expensive, allowed averaging a larger number of turbulent structures than the smaller one. Therefore, each ETT computed in the higher *Re* case contains more information towards calculating statistics. This example highlights the interest of using the normalized ETT* definitions (5) and (6). This also helps to compare, in a more objective way, statistics from different databases performed in various computational boxes.

The results summarized in Table 3 are presented graphically in Fig. 1. The first interesting conclusion that can be drawn is the fact that, although Moser et al. [27] and del Álamo [28] in principle used the same criterion for convergence, they reach very different convergence levels. The database from Jiménez's research group [2, 38, 39] shows a consistent level of convergence throughout the whole Reynolds number range, on the order of $\varepsilon \simeq 10^{-3}$, which can be considered to be sufficiently converged. However, the runs by Moser et al. [27] exhibit convergence indicators on the order of 4–10 times larger than the ones by Jiménez. This indicates the need for an objective convergence criterion that allows for comparisons between simulations. It is also interesting to note that Kim et al. [1] actually reach a convergence level very similar to the one from Jiménez, and the database from Iwamoto et al. [29] exceeds their convergence level by several orders of magnitude at low *Re*.

With respect to the results shown in Fig. 1b, it is important to see that Iwamoto et al. [29] achieved such well converged results by running for much longer periods than the other research groups. Also, Kim et al. [1] reached similar levels of convergence to the ones of Jiménez running for a much shorter period. A possible explanation of this fact is discussed in Sect. 3, where we assess the influence of the spacing in time between individual samples used to compute statistics, Δt. It is also important to note the fact that the

Table 3 Convergence features of channel flows in the literature

DNS database	Re_τ	ETT_S	ETT_A	ETT_S^*	ETT_A^*	$\varepsilon_{channel}$
Kim et al. [1]	180	–	10	–	43.9	1.88×10^{-3}
Moser et al. [27]	392	–	–	–	–	4.80×10^{-3}
	587	–	–	–	–	8.50×10^{-3}
Iwamoto et al. [29]	109	–	2559	–	14,031	1.03×10^{-5}
	150	–	2061	–	11,300	2.91×10^{-5}
	298	–	277	–	379.7	6.61×10^{-5}
	396	–	129	–	176.8	9.38×10^{-4}
	643	–	40	–	54.8	1.67×10^{-3}
del Álamo et al. [39]	186	–	52.8	–	922.4	1.27×10^{-3}
	547	–	13.7	–	239.7	1.11×10^{-3}
del Álamo et al. [2]	934	–	11.7	–	153.5	1.08×10^{-3}
Hoyas and Jiménez [38]	2004	–	10.3	–	135.5	7.73×10^{-4}
Tuerke [30]	550	5	–	5.5	–	–
	950	5	–	5.5	–	–

Table 4 Convergence features of duct flows in the literature

DNS database	$\overline{Re_\tau}$	ETT_S	ETT_A	ETT_S^*	ETT_A^*	ε_{duct}
Gavrilakis [31]	150	6	5	62.8	52.3	3.27×10^{-3}
Huser and Biringen [32]	300	120	30	256	64	2.97×10^{-3}
Uhlmann et al. [34]	78	–	60.8	–	127.4	1.30×10^{-2}
	100	–	108.8	–	113.9	2.02×10^{-2}
Pinelli et al. [33]	150	–	544.2	–	1,139.8	2.02×10^{-3}
	230	–	377.4	–	790.4	1.77×10^{-3}
Ohlsson et al. [40]	310 (AR = 3.33)	12.1	17.5	–	–	–
Krasnov et al. [36]	4253	–	1.3	–	2.7	–

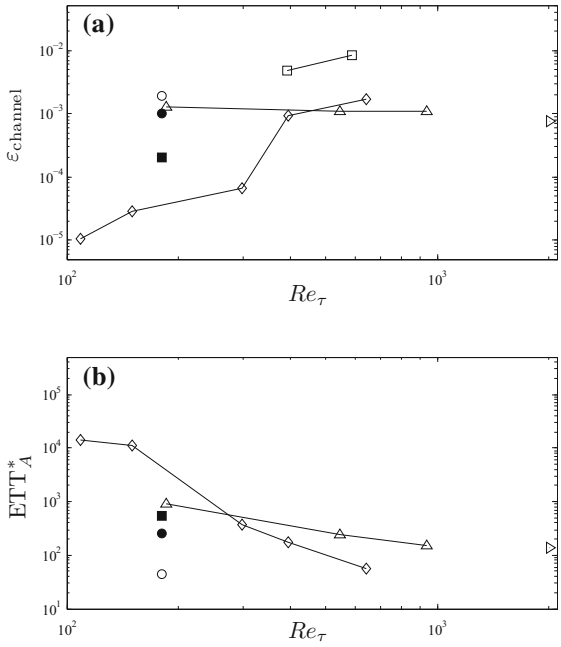

Fig. 1 **a** Convergence indicator and **b** averaging time expressed in ETT* with correction for box size, both as a function of friction Reynolds number, for channel flow DNSs available in the literature and run from the present study. *Symbols* correspond to the following databases: *open circle* Kim et al. [1], *open square* Moser et al. [27], *open Diamond* Iwamoto et al. [29], *open triangle* del Álamo et al. [2, 39], *open right pointed triangle* Hoyas and Jiménez [38], *filled circle* present (short T_A), *filled square* present (long T_A)

averaging time required to obtain converged statistics seems to exhibit a decreasing trend with Reynolds number, showing a difference of a whole order of magnitude between Re_τ values of 180 and 2000.

With respect to duct literature, a summary of the convergence results obtained from available data is given in Table 4. Most available computations correspond to square ducts (except for the aspect ratio 3.33 duct preceding a three-dimensional diffuser computed by Ohlson et al. [40]) at low Reynolds numbers. The only exception is the very high *Re* case by Krasnov et al. [36], which will be discussed later. The duct cases require very long averaging times for convergence due to the interaction between the secondary motions produced at the duct corners and the mean flow. This interaction has been extensively studied experimentally by Gessner et al. [41] and Gessner and Jones [42], and numerically by Vinuesa et al. [43]. Despite this, in Table 4 only Pinelli et al. [33] averaged for long periods of time. This is in part due to the lack of a consistent convergence criterion for ducts (the linear total shear profile criterion is not valid as we discussed above), and partly because duct cases are much more expensive than the periodic channel. The presence of two inhomogeneous directions does not allow the use of periodic boundary conditions in the spanwise direction, a fact that significantly increases computational cost. Another detail must be highlighted when comparing Tables 3 and 4: the convergence indicators $\varepsilon_{channel}$ and ε_{duct} are not defined in terms of the same physical magnitude (shear stress for the former, and momentum in the latter), although both are expressed in nondimensional form.

Figure 2 shows with open symbols the convergence properties of available duct flows as a function of Reynolds number. The threshold for convergence can be established on an ε_{duct} value of around 10^{-3}, a level which is not fully reached by any of the available datasets. The very long runs by Pinelli et al. [33] show the lowest ε values, around 2×10^{-3}. On the next level of convergence we would find the runs by Gavrilakis [31] and Huser and Biringen [32], partly converged, with convergence indicators around $\varepsilon \simeq 3 \times 10^{-3}$. It is interesting to see how they exhibit very similar ETT_A^*

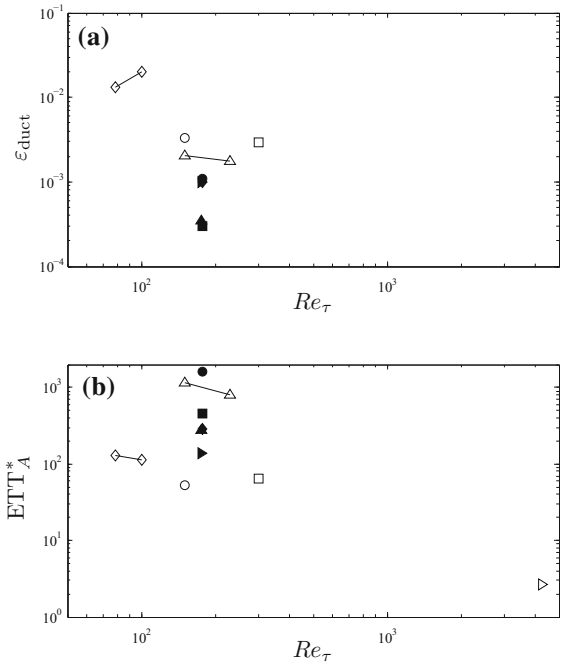

Fig. 2 **a** Convergence indicator and **b** averaging time expressed in ETT* with correction for box size, both as a function of friction Reynolds number, for duct flow DNSs available in the literature and runs from the present study (represented by full symbols). *Symbols* correspond to the following databases: *open circle* Gavrilakis [31], *open square* Huser and Biringen [32], *open diamond* Uhlmann et al. [34], *open triangle* Pinelli et al. [33], *open right pointed triangle* Krasnov et al. [36], *filled circle* present AR = 1, *filled square* present AR = 3 (long T_A), *filled diamond* Present AR = 3 (short T_A), *filled triangle* Present AR = 5 (long T_A) and *filled right pointed triangle* Present AR = 5 (short T_A)

values, with also consistent convergence indicators, although Gavrilakis' runs were averaged for a very short period of time ($ETT_A = 5$ vs. 30 from Huser and Biringen) if the box size correction is not applied. Gavrilakis used a very long computational box (L_x was 20π), which is why the correction brings the averaging periods from both runs very close. This is in agreement with our previous discussion, and highlights the importance of the correction for box size. The case of Uhlmann et al. [34] seems more surprising, since their averaging time is longer than the ones from Gavrilakis and Huser and Biringen, but they show quite large values of ε_{duct}. This is because they computed very low Reynolds numbers, which lie in what they call "marginally turbulent state", and therefore require even longer averaging times than a fully-turbulent square duct flow. The last case, the very high-*Re* computation by Krasnov et al. [36], presents a very short averaging time (around 30 times shorter than Pinelli's values extrapolated to such a high Reynolds number). We did not have access to their database, so we were unable to calculate their convergence indicator, although they mention in their study [36] some problems in their statistics which they attribute to short averaging periods. In addition, their second-order finite-difference code may not provide as much accuracy as the spectral or fourth order finite-difference codes proposed by other research groups, especially at such high *Re*.

3 Direct numerical simulations of turbulent channel and ducts flows

After carefully reviewing previously proposed convergence criteria, and assessing the level of convergence from available DNSs, we performed our own direct numerical simulations of one channel flow, and analyzed existing duct flow data with aspect ratios 1, 3 and 5 [26]. All the cases were computed at Re_τ values around 180 (in the case of the ducts, the flow was adapted as discussed below to maintain the same conditions at the centerplane for the various aspect ratios). The results of these computations are shown on Figs. 1 and 2 using filled symbols. The characteristics of the numerical codes and the computations are presented next.

3.1 DNS of turbulent channel flow

Direct numerical simulations require computing all the spatial and temporal scales of the flow, including the largest energy-containing and the smallest dissipative ones. To that end, the computational mesh needs to be very fine close to the walls (in order to properly capture the smallest scales, which reside in the near-wall region), and it is coarsened as the core of the flow is approached, where the larger scales reside. For adequate simulation reliability, the numerical discretization has to allow an accurate representation of all the flow scales. Thus, high-order numerical schemes are the preferred methods for turbulence.

The numerical computation of turbulent channel flow was carried out using the numerical code SIMSON [44], based on a pseudo-spectral discretization to solve the three-dimensional, time-dependent,

incompressible Navier–Stokes equations. Periodic boundary conditions are used in the streamwise and spanwise directions, where Fourier expansions with dealiasing represent the velocity field, and Chebyshev polynomials were used in the wall-normal direction. The streamwise pressure gradient was recalculated after each time-step to maintain a constant mass flux through the channel cross-section. The kinematic viscosity ν was set so that a Reynolds number based on channel half-height h and bulk velocity U_b of $Re_b \simeq 2800$ was obtained; this led to a friction Reynolds number of $Re_\tau \simeq 180$. In this code, time is advanced by means of a standard mixed four-step Crank–Nicolson/Runge–Kutta scheme.

The computational box was the same as in Kim et al. [1], i.e., streamwise and spanwise lengths of $L_x = 4\pi$ and $L_z = 2\pi$, with wall-normal length $L_y = 2$. Uniform grid spacings of $\Delta x^+ = 12$ and $\Delta z^+ = 7$ were kept in the homogeneous directions, whereas the Chebyshev distribution in the wall-normal direction led to a minimum grid spacing of $\Delta y^+_{\text{min}} = 0.05$ at the wall, and a maximum $\Delta y^+_{\text{max}} = 4.4$ at the channel core. A total of $192 \times 129 \times 160$ grid-points in the x, y and z directions were considered to discretize the computational domain. The simulation is initiated with random noise at $t = 0$.

In order to identify adequate values of T_S and T_A, we generate a contour map with a wide range of (T_S, T_A) combinations obtained from the channel simulation, and plot the value of $\varepsilon_{\text{channel}}$, which should ideally decay to zero as statistical convergence is approached. However, only few of the runs by Iwamoto et al. [29] exhibit converge indicators below 10^{-3}, and most of the runs from Jiménez's group are close to this value. Since for practical purposes, statistics obtained with $\varepsilon_{\text{channel}} = 10^{-3}$ can be considered to be sufficiently converged, we will take this as our convergence criterion for channel flows. The contour plot of $\varepsilon_{\text{channel}}$ versus the starting and averaging times T_S and T_A in convective time units (nondimensionalized using U_b and h) is shown in Fig. 3 for our channel flow simulation. This figure shows how, for starting times lower than approximately 200 convective time units, the value of ε decays very slowly, even for increasingly longer averaging times. This is due to the fact that, for $T_S < 200$, the instantaneous flow is not representative of a physical turbulent field, and therefore should not be accounted for in the flow statistics. Interestingly, for starting times larger than 200 convective time units (equivalent to $\text{ETT}^*_S = 50$), the value of the convergence indicator starts to decay more quickly with averaging time.

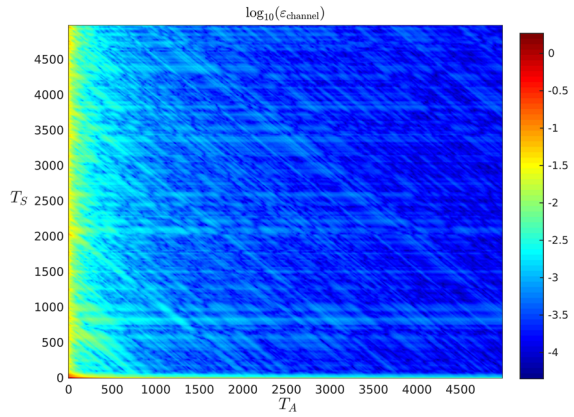

Fig. 3 Contour plot of channel convergence indicator in logarithmic scale, $\log_{10}(\varepsilon_{\text{channel}})$, versus starting and averaging times in convective time units, i.e., nondimensionalized using bulk velocity U_b and channel half-height h. Data extracted from DNS carried out in the present study

Figure 4 shows, for $T_S = 200$ convective time units, the value of $\varepsilon_{\text{channel}}$ as a function of the averaging time T_A. Note that the effect of the separation in time Δt between individual realizations used to compute the statistics is also explored in Fig. 4, where the lowest value $\Delta t = 0.2$ was precisely the one used to generate the contour plot in Fig. 3. The first conclusion obtained from this figure is the fact that the value of Δt plays a role in the necessary averaging time T_A for convergence. Whereas values of $\Delta t = 5$ or 10 lead to slower decays of $\varepsilon_{\text{channel}}$, the value $\Delta t = 2$ (corresponding to $\Delta t^+ = 17$ in this simulation) essentially yields the same decay rate as the value of 0.2 considered in Fig. 3, and therefore suggests that convergence not only depends on the combination of T_A and T_S, but also on Δt. This figure indicates that, assuming $\Delta t = 2$, convergence indicators below 10^{-3} are obtained with a minimum averaging time of around 1000 convective time units, which in eddy turnover times leads to $\text{ETT}_A = 57$, and after box size correction results in $\text{ETT}^*_A = 250$. ε values of 2×10^{-4} can be achieved with $T_A \simeq 2200, \text{ETT}_A = 125.4$ and $\text{ETT}^*_A = 550$. These results are compared with the rest of data in Fig. 1, where the ε cases of 10^{-3} and 2×10^{-4} are denoted by "short T_A" and "long T_A" respectively.

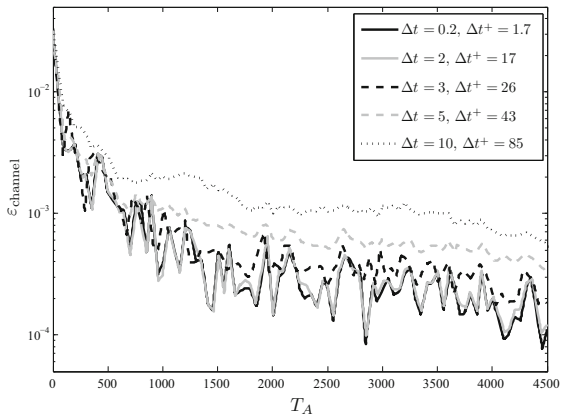

Fig. 4 Channel convergence indicator $\varepsilon_{\text{channel}}$ versus averaging time with starting time $T_S = 200$. Several values for the separation in time Δt between realizations used to compute the statistics are shown, with $\Delta t = 0.2$ being the one used to generate Fig. 3. Times expressed in convective time units, and data extracted from DNS carried out in the present study

The short T_A run exhibits levels of convergence similar to the ones of del Álamo et al. and Kim et al. although the averaging time (corrected for box size) lies in between. With respect to the long T_A run, lower $\varepsilon_{\text{channel}}$ levels than the ones from del Álamo et al. are obtained, with shorter averaging times. A plausible explanation for this discrepancy could be the different values of Δt (for which there is no information in the respective references), which as discussed below directly impact the rate at which convergence is reached. Given the results shown in Fig. 4, Δt^+ values equal to or below 17 should be considered in order to obtain proper convergence rates.

3.2 DNSs of turbulent duct flows

Like in the channel flow case, a direct numerical simulation technique was used to compute turbulent duct flows at three different aspect ratios. These simulations were carried out using the code Nek5000, developed by Fischer et al. [45] at Argonne National Laboratory (nek5000.mcs.anl.gov), and based on the spectral element method (SEM), originally proposed by Patera [46]. In this code, the incompressible Navier–Stokes equations are cast in weak form, so they are multiplied by a test function and integrated over the domain. The Galerkin approximation is considered for spatial discretization following the $\mathbb{P}_N - \mathbb{P}_{N-2}$ formulation by Maday and Patera [47], that associates the pressure with polynomials two degrees lower than the velocity. The three-dimensional velocity vector is expressed in terms of tensor-products of Lagrange polynomials of order N within a spectral element, and the solution is represented at the Gauss-Lobatto-Legendre (GLL) quadrature points. The nonlinear terms are treated explicitly by third order extrapolation (EXT3), whereas the viscous terms are treated implicitly by a third-order backward differentiation scheme (BDF3) leading to a linear symmetric Stokes system to be solved at every time step.

These computations were carried out on a Cray XE6 machine at the PDC Center of KTH in Stockholm (Sweden). They required from 2048 to 4096 cores, and the MPI (message-passing interface) was employed for parallelization. In all the cases, the computational box was 25 duct half-heights long ($L_x = 25h$). This is large enough to capture the longest turbulent structures in the streamwise direction according to experimental measurements in pipe flow (Guala et al. [48]) and DNSs of turbulent channel (Jiménez and Hoyas [49]) and pipe flows (Chin et al. [50]). The box length in the wall-normal direction is $L_y = 2h$ for all cases, and the spanwise length is adjusted depending on the aspect ratio, so for AR = 5 we have $L_z = 10h$. The mesh is designed so that $\Delta x^+ < 10, \Delta y^+_{\text{max}} < 5$, and we have at least 4 points below $y^+ = 1$ (the guidelines for y also apply to z). Although the nodes within spectral elements are the GLL quadrature points, one has freedom to choose the element distribution, so we blended Chebyshev (close to the wall) with uniform (at the duct core) distributions, satisfying the various mesh quality requirements. Also, in an approach similar the one considered for the channel, here we adjust the input Reynolds number Re_b through an iterative process, in order to keep the centerplane bulk Reynolds number $Re_{b,c} = U_{b,c}h/\nu$ (where $U_{b,c}$ is the bulk velocity at the centerplane of the duct) constant for the different aspect ratios. This allows easier comparisons among aspect ratio cases and with available channel data. Therefore, the nominal Re_τ values are just a reference, since the actual $Re_{\tau,c}$ will change with AR. Note that the flow is allowed to approach fully-developed turbulence via consecutively more refined runs, and the initial profile was a laminar duct flow expansion [51] with a wall-normal volume force tripping (which is activated only during

the initial low-resolution runs) similar to the one used by Schlatter and Örlü [19].

3.2.1 Results from the square duct case

A contour plot of $\log_{10}(\varepsilon_{\text{duct}})$ in terms of T_A and T_S (both in convective time units) is shown in Fig. 5 for the xy centerplane (note that the xz plot looks qualitatively very similar). In this figure we represent data up to 1680 convective time units only, which is enough to identify the initial transients: in the xy centerplane the region of lowest ε can be found for $T_S \simeq 100$, and averaging times of around 1580. This would not be the lowest possible ε value, and it is necessary to look at the complete time history (starting from $T_S = 100$) to identify the minimum T_A to ensure convergence. This is done in Fig. 6, where ε_{xy} and ε_{xz} are shown as a function of averaging time. Note that in the present turbulent duct simulations Δt was kept below 0.2 in all cases. It can be observed how after an initial averaging period of 1000 convective time units, the decay in ε is very slow. This is related to the interaction between the secondary flow with the mean flow, and it can be argued that stationary behavior will require really long averaging times in this flow. However, reasonable levels of convergence should be sufficient for reliable conclusions. The minimum ε is around 10^{-3} in both centerplanes. From Fig. 6, this

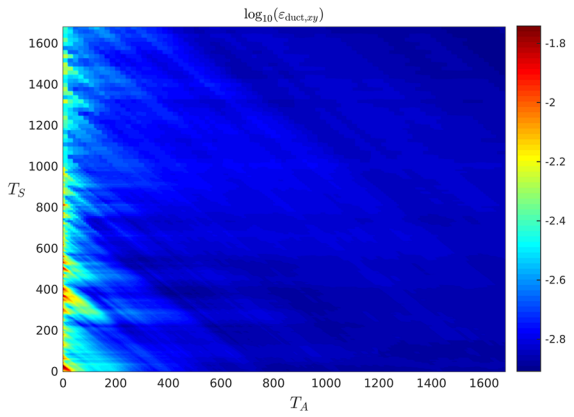

Fig. 5 Contour plot of duct convergence indicator in logarithmic scale calculated in the xy centerplane, $\log_{10}(\varepsilon_{\text{duct},xy})$, versus starting and averaging times in convective time units, i.e., nondimensionalized using bulk velocity U_b and duct half-height h. Data extracted from DNS simulation of AR = 1 duct flow carried out in the present study

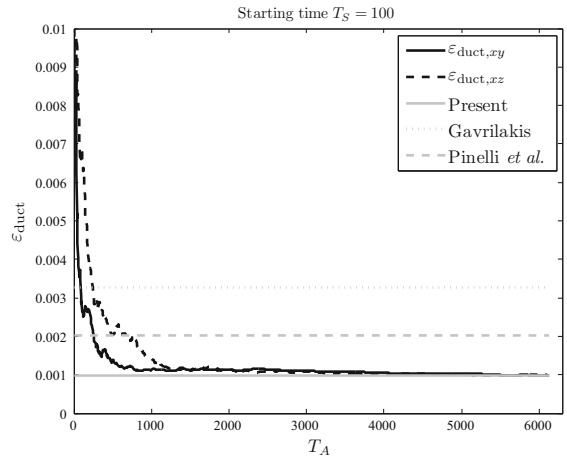

Fig. 6 Duct convergence indicator $\varepsilon_{\text{duct}}$ from xy and xz centerplanes, versus averaging time with starting time $T_S = 100$. Times expressed in convective time units, and data extracted from DNS simulation carried out in the present study. Comparison with convergence data extracted from the simulations by Gavrilakis [31] and Pinelli et al. [33] are also shown

value is not reached by the average ε curve until around $T_A = 5400$ convective time units. As a consequence, we can argue that, in order to reach sufficient statistical convergence ($\varepsilon_{\text{duct}} \simeq 10^{-3}$), we need to discard 100 convective time units of initial transients (equivalent to $\text{ETT}_S = 7.12$ and $\text{ETT}^*_S = 30$ in our simulation), and then average for at least 5400 convective time units (equal to $\text{ETT}_\text{A} = 385$ and $\text{ETT}^*_A = 1602$).

3.2.2 Results from the AR = 3 duct case

Figure 7 shows the contour of $\log_{10}(\varepsilon_{\text{duct}})$ evaluated at the xy centerplane, as a function of starting and averaging times. This figure shows that transient effects are present until $T_S = 200$, which is equivalent to $\text{ETT}_\text{S} = 13.8$, or $\text{ETT}^*_\text{S} = 57.5$) if the box size correction is considered. The minimum ε value is obtained at approximately $T_A = 1600$, which corresponds to $\text{ETT}_A = 110$ and $\text{ETT}^*_A = 460$. Although the minimum $\varepsilon_{\text{duct}}$ is 2.95×10^{-4}, a more moderate convergence value of $\varepsilon_{\text{duct}} = 10^{-3}$ can be obtained with $T_A = 1000$ or $\text{ETT}^*_A = 287.5$. It is also interesting to note that the convergence indicator on the xz centerplane reaches a value of $\varepsilon = 1.5 \times 10^{-3}$ rather quickly (T_A of around 200), but then this indicator does

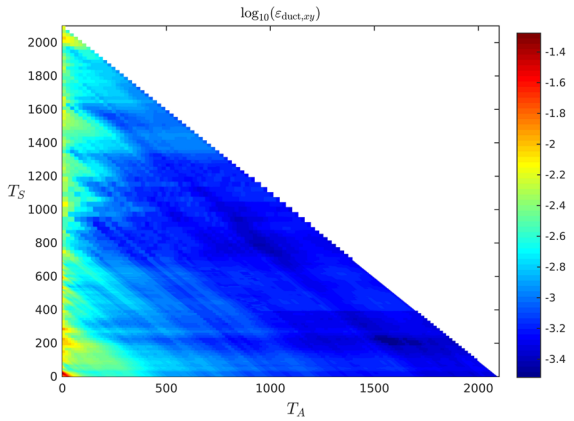

Fig. 7 Contour plot of duct convergence indicator in logarithmic scale calculated at the *xy* centerplane, $\log_{10}(\varepsilon_{\text{duct},xy})$, versus starting and averaging times in convective time units, i.e., nondimensionalized using bulk velocity U_b and duct half-height h. Data extracted from DNS simulation of aspect ratio 3 duct flow carried out in the present study. *Note* that the white region in *upper right* half of the figure is associated with the fact the database analyzed to produce this figure contained data up to $t = 2100$, and therefore T_S values larger than 0 lead to T_A values smaller than 2100

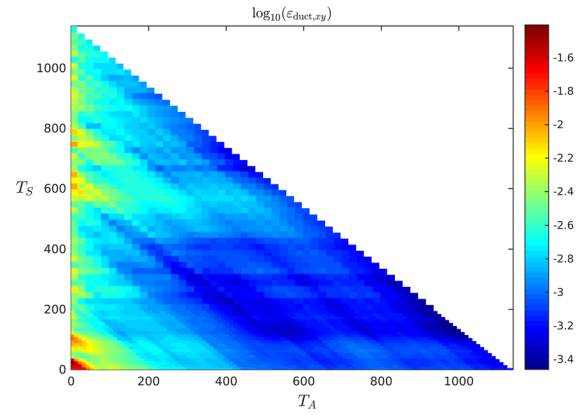

Fig. 8 Contour plot of duct convergence indicator in logarithmic scale calculated in the *xy* centerplane, $\log_{10}(\varepsilon_{\text{duct},xy})$, versus starting and averaging times in convective time units, i.e., nondimensionalized using bulk velocity U_b and duct half-height h. Data extracted from DNS of aspect ratio 5 duct flow carried out in the present study. Note that the *white region* in *upper right* half of the figure is associated with the fact the database analyzed to produce this figure contained data up to $t = 1140$, and therefore T_S values larger than 0 lead to T_A values smaller than 1140

not get significantly smaller. This is associated with the fact that the most significant physical mechanisms take place on the *xy* centerplane instead of the spanwise direction.

3.2.3 Results from the AR = 5 duct case

Figure 8 shows the $\varepsilon_{\text{duct}}$ contours for all the T_A and T_S combinations, and a starting time $T_S = 100$ (similar to what one observed when analyzing the time evolution of $Re_{b,c}$), equal to 6.75 eddy turnover times, and 28 after box-size correction appears suitable. With respect to averaging periods, the best convergence is reached with $T_A = 1000$ ($\text{ETT}_A = 67.5$ and $\text{ETT}_A^* = 280$), which leads to $\varepsilon_{\text{duct}} = 3.46 \times 10^{-4}$, although a more moderate level of convergence of 10^{-3} can be obtained with $T_A = 500$ (or $\text{ETT}_A^* = 140$).

The convergence and averaging time results from the previous sections are also summarized in Fig. 2, where a comparison with the available data in the literature is also shown. Note that for the aspect ratio 3 and 5 cases we present two scenarios: the short T_A (which should be considered as a minimum requirement for convergence) and the long T_A (corresponding to our longest runs, with the lowest possible convergence indicators).

4 Characterization of the mean cross-flow structure in turbulent rectangular ducts

4.1 Vortex identification methods

A number of methods are available in the literature to determine the location of coherent structures in turbulent flows, among which some of the most popular are the Q criterion by Hunt et al. [52], the Δ criterion proposed by Chong et al. [53], the swirling strength condition by Zhou et al. [54], the approach by Kida and Miura [55] and the λ_2 method by Jeong and Hussain [25]. We have extensively tested all these methodologies and found that all of them yield very similar results. The analysis presented in Sect. 4.2 was performed by considering the λ_2 method [25], which as most vortex identification methods, is based on the analysis of the properties of the velocity gradient tensor:

$$\nabla \mathbf{u} = \begin{bmatrix} u_x & u_y & u_z \\ v_x & v_y & v_z \\ w_x & w_y & w_z \end{bmatrix}, \tag{7}$$

where all the velocities in (7) are instantaneous and $u_x = \partial u/\partial x$, etc. Note that this tensor can be decomposed into the symmetric and antisymmetric parts $S =$

$1/2(\nabla u + \nabla u^T)$ and $\Omega = 1/2(\nabla u - \nabla u^T)$, respectively. The λ_2 criterion [25] is based on the observation that if one neglects the viscous and unsteady effects, the following equation can be derived by taking the gradient of the incompressible Navier–Stokes equation:

$$S^2 + \Omega^2 = -\frac{1}{\rho}\nabla(\nabla p), \tag{8}$$

which implies that based on velocity gradient tensor properties (S and Ω) one can find the regions of local pressure minimum associated with vortex centers. Jeong and Hussain [25] define a vortex core as a region where $S^2 + \Omega^2$ has two negative eigenvalues. Therefore, it is sufficient to sort the eigenvalues in increasing order and check the sign of the second one (which gives the λ_2 name to the method).

4.2 Characterization of the secondary flow

In this section we analyze the in-plane structure of the flow in turbulent square ducts at $Re_{\tau,c} \simeq 180$ and 360, and of rectangular ducts with aspect ratios 3 and 10 at $Re_{\tau,c} \simeq 180$. The databases considered for these analyses are described in detail in Refs. [26, 43]. In Fig. 9 we assess the Reynolds-number effects on the flow by analyzing streamwise velocity U, streamlines of the mean secondary flow ψ, probability density function (pdf) of coherent vortex locations obtained with the λ_2 method [25] and mean streamwise vorticity Ω_x. The first interesting feature of the flow at the two Reynolds numbers is the fact that the typical secondary flow pattern with one pair of counter-rotating vortex on each corner can be observed. This type of cross-flow is denoted as secondary flow of second kind [56], and it is formed by the cross-stream Reynolds stress difference $\overline{v^2} - \overline{w^2}$ and the deviatoric Reynolds shear stress $\overline{vw}$. It is clear from both parts of the figure that the secondary flow basically convects momentum from the duct centerplane towards the duct bisector, and the iso-contours of the streamwise velocity reflect this effect: the flow is lifted at $z/h \simeq 0$ (with the corresponding local reduction of wall shear stress), and pushed towards the corner along the duct bisector. It is also interesting to note that the pdf of vortex locations follows the distribution of iso-

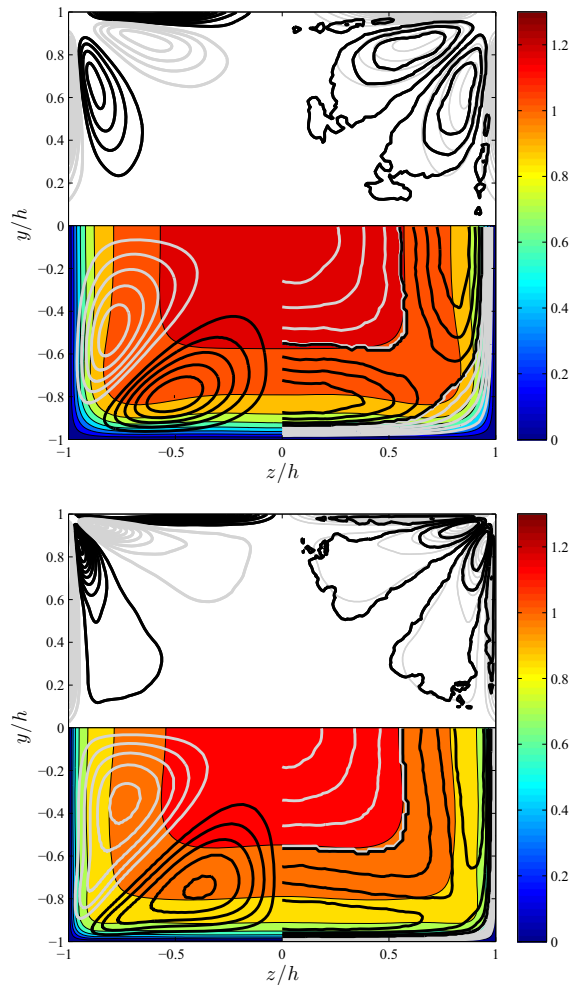

Fig. 9 In-plane flow in square ducts at (*top*) $Re_{\tau,c} \simeq 180$ and (*bottom*) $Re_{\tau,c} \simeq 360$. The lower half shows the streamwise velocity U; the *lower-left* quadrant shows streamlines of secondary mean flow ψ, where the *grey lines* correspond to clockwise sense of rotation, and *black lines* to anticlockwise (10 contours with increments of 3.9×10^{-4}); the *lower-right* quadrant shows the pdf of vortex location obtained with the λ_2 criterion [25], where *grey lines* indicated probability less than 60 % of the maximum probability of occurrence, and *black lines* higher probability (10 contours with increments of 10 %); the upper-left quadrant shows mean streamwise vorticity Ω_x, where the *grey lines* indicate negative vorticity and the black lines positive one (20 contours, with increments of 0.07); and upper-right corner shows in *grey* the Ω_x field, and in *black* the difference between the pdf of vortex locations with positive and negative streamwise vorticity (6 contours, with increments of 16.67 %). Note that these fields were averaged in time, streamwise direction, and over the four quadrants of the duct, and that U_b and h were considered as velocity and length scales, respectively

contours of the mean flow as well, which further supports the connection between the individual vortical structures and the averaged flow features. The two thick black lines indicate the separation between regions with probability above and below 60 % of the maximum probability of occurrence, and as expected the probability decreases as the core of the flow and the wall are approached. The corner region also exhibits a very low probability of vortex occurrence due to the inhibiting effect of the side wall on the turbulent cycle taking place on the horizontal wall (and viceversa), which leads locally to very low *Re* conditions. With respect to the regions of high probability of finding vortices, in both cases the maximum probability is obtained at a wall-normal distance of around 40^+, which is in agreement with the square duct simulations by Pinelli et al. [33] up to $Re_\tau \simeq 300$ (based on friction velocity averaged over the four walls). Note that in the study by Pinelli et al. [33] the pdf of streak locations was evaluated by means of the wall shear stress time history, whereas here we reach the same conclusion based on the analysis of individual vortical structures. Although the location of maximum pdf is fixed in inner units, in outer units this location is $y/h \simeq 0.22$ and $\simeq 0.11$ in the low and high-*Re* cases respectively, which shows the effect of a wider scale separation as consequence of the increasing Reynolds number. This is also manifested in the vortex distributions, where the region of low pdf remains bounded to a narrower region close to the wall in the higher *Re* case. Another interesting effect of the Reynolds number is the fact that the inner-scaled duct widths are $\simeq 360$ and 720 respectively, which limits the number of streaks present in each case since the spanwise separation between two adjacent streaks is approximately 50^+.

With respect to the streamlines of the secondary flow shown in Fig. 9, both *Re* cases exhibit similar features although the pattern in the $Re_{\tau,c} \simeq 360$ case appears to be more stretched towards the core, as also observed by Pinelli et al. [33]. Interestingly, the centers of the vortices also move farther away from the wall as *Re* increases, which suggests that large-scale structures in the flow play an important role in the formation of the secondary flow. The opposite effect is observed in the streamwise vorticity pattern: although qualitatively the Ω_x fields share some features with the ψ one (namely the sense of rotation from the duct centerplane towards the bisectors). On the other hand as *Re* increases, in the case of the wall vorticity component of opposite sign, the vorticity field contracts and becomes limited to a progressively smaller region closer to the wall. The centers of the Ω_x regions also move towards the wall for increasing Reynolds numbers, which indicates that the near-wall structures are more relevant to the streamwise vorticity field than the large-scale motions. This is further corroborated when analyzing the difference between the pdf of occurrence of vortices with positive and negative streamwise vorticity, which was also analyzed by Pinelli et al. [33], and strongly resembles the Ω_x field. Note that a total of 100 instantaneous fields of streamwise length $L_x = 25h$ were analyzed to obtain these results, and a larger number of fields would allow one to detect more individual structures, which would likely lead to better agreement with the Ω_x field. These results demonstrate that there is a strong connection between the individual vortical structures preferentially located close to the corner and the streamwise vorticity field, which explains why Ω_x contracts for increasing *Re*. It can therefore be argued that the streamline field scales in outer units whereas the streamwise vorticity one does it in inner units, hence highlighting the complex and multiscale nature of the secondary flow of second kind.

The assessment of Reynolds-number effects presented above is complemented with an analysis of the impact of aspect ratio at $Re_{\tau,c} \simeq 180$, where Fig. 10 shows the same quantities as before for AR = 3 and 10. Note that in the rectangular ducts the streamwise velocity field reflects the effect of the secondary flow through the deformation of the iso-contours, especially at the corners. Since the Reynolds number is the same, the region of highest probability of vortex occurrence is $y/h \simeq 0.22$ in both cases, corresponding to $y^+ \simeq 40$ as in the square duct. Also note how the much wider inner-scaled widths of these ducts ($\simeq 1,080^+$ and $\simeq 3,600^+$) lead to a larger number of streaks on the horizontal walls. Although the geometry determines the behavior of the near-wall streaks close to the corner, as the core of the duct is approached the distribution is progressively more homogeneous. The streamline pattern also exhibits an interesting behavior with increasing aspect ratio: when transitioning from the square duct to the AR = 3 case, the vortex closer to the corner gets slightly constrained, whereas the vortex positioned on the

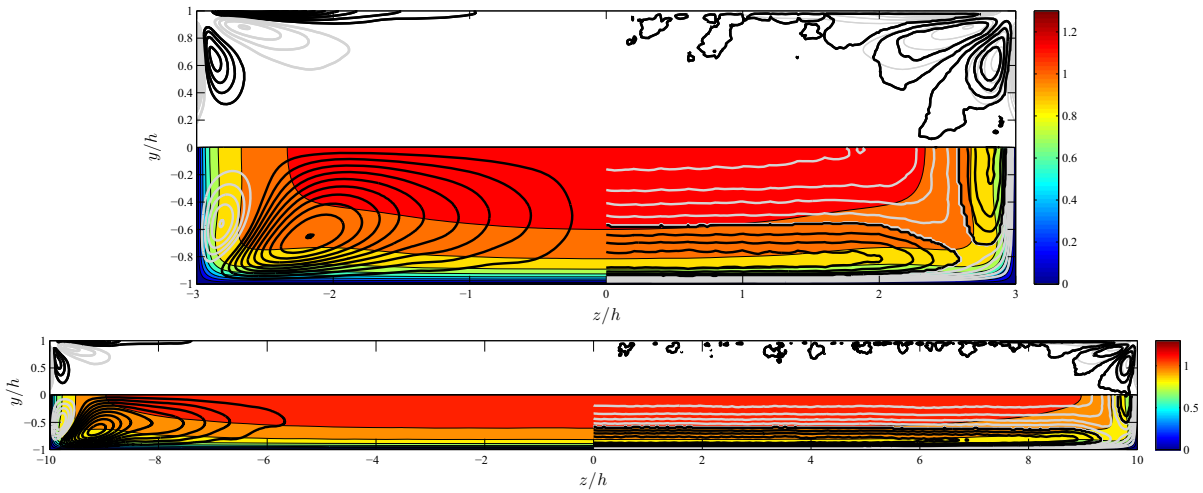

Fig. 10 In-plane flow in (*top*) AR = 3 and (*bottom*) AR = 10 ducts at $Re_{\tau,c} \simeq 180$. Same quantities as in Fig. 9, with the exception that here we consider a total of 15 contours of ψ instead of 10, also with increments of 3.9×10^{-4}

horizontal wall significantly expands in z, all the way to the centerplane. Its center also moves slightly away from the corner, from a distance of around $0.5h$ in the square duct to around $0.8h$. Further increase of the aspect ratio produces a progressive development of the vortex on the horizontal wall, up to a spanwise distance of around $5h$ from the corner, although its center appears to remain at a distance of $0.8h$ from the corner. This is another manifestation of the relevance of large-scale motions in the flow on the streamline pattern: in this case larger scales are allowed by the physical increase of the spanwise dimension, instead of the larger scale disparity produced by a higher Re. A very interesting observation can be drawn from the Ω_x fields: the region closer to the corner does not get constrained as the aspect ratio is increased, and the region next to it expands to a much lower extent than the streamline pattern in the AR = 3 and 10 cases. In this regard, the vorticity component along the horizontal wall shows more development in z, but still not as much as the streamlines. Note that the center of the vorticity region closer to the corer remains constant at a distance of around $0.1h$ as AR increases, and it is quite remarkable that the region next to it, unlike the streamline pattern, also has a fixed center located at a distance of around $0.3h$. Therefore, the larger scales resulting from a physically wider duct do not significantly affect the fundamental behavior of the streamwise vorticity field, since its relevant physics are associated with the near-wall structures. The difference between the pdf of occurrence of vortices with positive and negative streamwise vorticity, which also in these cases shows strong resemblance with the Ω_x field, further reinforces this conclusion. The analysis of coherent structures was based on 334 instantaneous fields in the AR = 3 case and 536 in the AR = 10 one.

5 Conclusions and discussion

Despite the impact of convergence level on the final statistics of direct numerical simulations of wall-bounded turbulence, there is not a consistent criterion in the literature to allow appropriate convergence assessments. In this study a wide range of databases of turbulent channel and duct flows is analyzed, comparing numerical algorithms, starting and averaging times and achieved level of convergence. To this end, a convergence indicator for channel flows $\varepsilon_{\text{channel}}$ based on the deviation of the total shear stress from a linear profile is defined. An extension of this criterion for duct flows ($\varepsilon_{\text{duct}}$) is also proposed, and since the total shear stress does not have to be linear in ducts, we measure the deviation with respect to the streamwise momentum balance at the duct centerplane. Note that this criterion applies to convergence of the duct at the centerplane section, and not to other cross-flow effects taking place in the spanwise direction. In order to allow appropriate comparisons of starting and

averaging times among simulations, we express both in eddy turnover times and then apply a correction based on the box size. The motivation of this correction is to acknowledge the fact that simulations run on larger boxes effectively contain more turbulent structures (in the homogeneous directions), thus are approximately equivalent to longer runs in smaller boxes. Comparisons of the indicator and corrected averaging time for available data in the literature lead to consistent trends in the results, thus proving the validity of the proposed approach.

We also present results from DNSs of a turbulent channel flow, and three duct flows with aspect ratios 1, 3 and 5, all of them at $Re_{\tau,c} \simeq 180$. The aim of these simulations was to find optimum values of starting and averaging times (T_S and T_A respectively, when expressed in convective time units) for various flow cases. We also find a maximum value of the spacing in time between individual realizations, which in inner scaling takes the value $\Delta t^+ = 17$. For both channel and duct we identified the converged state as that where the corresponding convergence indicator ε took a value of 10^{-3} or lower. Under this criterion, most of the available channel-flow data in the literature can be considered as converged, except the database by Moser et al. [27] which is however close to convergence. With respect to the duct data, none of the literature data can be considered to be sufficiently converged. This is in part due to the lack of an appropriate definition of convergence for the duct, and also due to the extremely long averaging times required for square ducts at low Reynolds numbers. The methodology proposed here can serve as a baseline to design new simulations, assess the quality of already existing ones, and more importantly can help to interpret and scrutinize available DNS data in the literature, in the same way as experimentalists take into account details of the experimental setup when interpreting a particular dataset.

It is important to note that the proposed criteria are meant to provide a baseline comparison between databases, and an idea of the convergence level achieved in channel and duct-flow simulations. However, these criteria are focused on the mean momentum balance, and therefore do not provide a comprehensive assessment of convergence. For instance, convergence in terms of ε does not guarantee convergence in other quantities of interest such as spectra, two-point correlations or Reynolds-stress transport equations. Therefore, the present work should be considered as an initial effort towards defining more general convergence criteria. Moreover, we also acknowledge that many research groups assess statistical convergence in a number of ways that are not necessarily reported in their publications: for instance, they assess the evolution of quantities that should be statistically zero when convergence has been achieved (such as the mean spanwise velocity in turbulent channel flows), or they confirm that statistics computed from the second half of the averaging time are consistent with those calculated in terms of the first half (which prevents from statistics polluted by inadequately stationary data). Other remarkable efforts toward establishing good practices in statistical convergence are the statistical error analyses by Oliver et al. [20] and Hoyas and Jiménez [21], or the documentation of residuals in the mean momentum balance and the Reynolds-stress transport equations in the simulations by Lee and Moser [4].

In a second part of the study, the in-plane structure of the flow in turbulent ducts is assessed by analyzing square ducts at $Re_{\tau,c} \simeq 180$ and 360 and rectangular ducts with aspect ratios 3 and 10 at $Re_{\tau,c} \simeq 180$ [26, 43]. The effect of the secondary flow of second kind on the mean flow, i.e., convection of momentum from the duct centerplane to the bisectors, is observed in the iso-contours of streamwise velocity. Identification of coherent vortices using the λ_2 criterion [25] shows that near-wall streaks are located in all the duct cases at a wall-normal distance of $y^+ \simeq 40$ as in Pinelli et al. [33], and the probability of occurrence of a vortex at the corner is very low due to the inhibiting effect of the side wall. Moreover, we find that the streamline pattern becomes stretched towards the duct core at higher Re and towards the duct centerplane at higher AR; the centers of the vortices also move away from the wall in both cases, which highlights the relevant role of large-scale motions on the streamline pattern of the secondary flow. On the other hand, the streamwise vorticity field becomes compressed towards the duct corners as Re increases, and its changes are comparatively small for increasing AR. The connection between the Ω_x field and the near-wall structures is further illustrated by comparing vorticity contours with the difference between the pdf of occurrence of vortices with positive and negative

streamwise vorticity. These conclusions, i.e., outer-scale scaling of ψ and inner-scale scaling of Ω_x, extend the findings by Pinelli et al. [33] to higher Reynolds numbers, and more importantly to another kind of large-scale motions in the flow through the consideration of wider ducts. They also highlight the complex and multiscale nature of the secondary flow of second kind in turbulent duct flows.

Acknowledgements RV and PS acknowledge financial support from the Knut and Alice Wallenberg Foundation and the Swedish Research Council (Vetenskapsrådet). The simulations were performed on resources provided by the Swedish National Infrastructure for Computing (SNIC) at PDC in Stockholm. We are also grateful to the various research groups who made their databases publicly available online.

Compliance with ethical standards

Conflict of interest The authors declare that they have no conflict of interest.

References

1. Kim J, Moin P, Moser RD (1987) Turbulence statistics in fully developed channel flow at low reynolds number. J Fluid Mech 177:133
2. del Álamo JC, Jiménez J, Zandonade P, Moser RD (2004) Scaling of the energy spectra of turbulent channels. J Fluid Mech 500:135
3. Lozano-Durán A, Jiménez J (2014) Time-resolved evolution of coherent structures in turbulent channels: characterization of eddies and cascades. J Fluid Mech 759:432
4. Lee M, Moser RD (2015) Direct numerical simulation of turbulent channel flow up to $re_\tau = 5200$. J Fluid Mech 774:395
5. Schlatter P, Örlü R (2010) Assessment of direct numerical simulation data of turbulent boundary layers. J Fluid Mech 659:116
6. Sillero JA, Jiménez J, Moser RD (2013) One-point statistics for turbulent wall-bounded flows at reynolds numbers up to $\delta^+ \simeq 2000$. Phys Fluids 25:105102
7. Wu X, Moin P (2008) A direct numerical simulation study on the mean velocity characteristics in turbulent pipe flow. J Fluid Mech 608:81
8. El Khoury GK, Schlatter P, Noorani A, Fischer PF, Brethouwer G, Johansson AV (2013) Direct numerical simulation of turbulent pipe flow at moderately high reynolds numbers. Flow Turbul Combust 91:475
9. Österlund JM (1999) Experimental studies of zero pressure-gradient turbulent boundary layer flow. PhD Thesis, Royal Institute of Technology (KTH), Stockholm, Sweden
10. Nagib HM, Chauhan KA, Monkewitz PA (2007) Approach to an asymptotic state for zero pressure gradient turbulent boundary layers. Phil Trans R Soc A 365:755
11. Chauhan KA, Monkewitz PA, Nagib HM (2009) Criteria for assessing experiments in zero pressure gradient boundary layers. Fluid Dyn Res 41:021404
12. Vinuesa R, Schlatter P, Malm J, Mavriplis C, Henningson DS (2015) Direct numerical simulation of the flow around a wall-mounted square cylinder under various inflow conditions. J Turbul 16:555
13. Vinuesa R, Nagib HM (2016) Enhancing the accuracy of measurement techniques in high Reynolds number turbulent boundary layers for more representative comparison to their canonical representations. Eur J Mech B Fluids 55:300
14. Vinuesa R, Duncan RD, Nagib HM (2016) Alternative interpretation of the Superpipe data and motivation for CICLoPE: the effect of a decreasing viscous length scale. Eur J Mech B Fluids 58:109
15. Talamelli A, Bellani G, Rossetti A (2014) The "long pipe" in CICLoPE: A design for detailed turbulence measurements. In: Progress in Turbulence V, Proceedings in Physics. Springer, vol 149, p 127
16. Klewicki JC, Falco RE (1990) On accurately measuring statistics associated with small-scale structure in turbulent boundary layers using hot-wire probes. J Fluid Mech 219:119
17. Antonia RA, Satyaprakash BR, Hussain AKMF (1982) Statistics of fine-scale velocity in turbulent plane and circular jets. J Fluid Mech 119:55
18. Örlü R, Schlatter P (2013) Comparison of experiments and simulations for zero pressure gradient turbulent boundary layers at moderate Reynolds numbers. Exp Fluids 54:1547
19. Schlatter P, Örlü R (2012) Turbulent boundary layers at moderate reynolds numbers: inflow length and tripping effects. J Fluid Mech 710:5
20. Oliver TA, Malaya N, Ulerich R, Moser RD (2014) Estimating uncertainties in statistics computed from direct numerical simulation. Phys Fluids 26:035101
21. Hoyas S, Jiménez J (2008) Reynolds number effects on the reynolds-stress budgets in turbulent channels. Phys Fluids 20:101511
22. Thompson RL, Sampaio LEB, Bragança Alves FAV, Thais L, Mompean G (2016) A methodology to evaluate statistical errors in DNS data of plane channel flows. Comp Fluids 130:1
23. del Álamo JC, Jiménez J, Zandonade P, Moser RD (2006) Self-similar vortex clusters in the turbulent logarithmic region. J Fluid Mech 561:329
24. Lozano-Durán A, Flores O, Jiménez J (2011) The three-dimensional structure of momentum transfer in turbulent channels. J Fluid Mech 694:100
25. Jeong J, Hussain F (1995) On identification of a vortex. J Fluid Mech 285:69
26. Vinuesa R, Noorani A, Lozano-Durán A, El Khoury GK, Schlatter P, Fischer PF, Nagib HM (2014) Aspect ratio

effects in turbulent duct flows studied through direct numerical simulation. J Turbul 15:677
27. Moser RD, Kim J, Mansour NN (1999) Direct numerical simulation of turbulent channel flow up to $Re_\tau = 590$. Phys Fluids 11:943
28. del Álamo JC (2005) La organización a gran escala de canales turbulentos. PhD Thesis, Polytechnic University of Madrid, Spain
29. Iwamoto K, Suzuki Y, Kasagi N (2002) Reynolds number effect on wall turbulence: toward effective feedback control. Int J Heat Fluid Flow 23:678
30. Tuerke F (2011) An inverse rans simulation of a turbulent channel flow at moderate reynolds numbers. Final Project Report, Polytechnic University of Madrid (Spain) and Technische Universität Berlin (Germany)
31. Gavrilakis S (1992) Numerical simulation of low-reynolds-number turbulent flow through a straight square duct. J Fluid Mech 244:101
32. Huser A, Biringen S (1993) Direct numerical simulation of turbulent flow in a square duct. J Fluid Mech 257:65
33. Pinelli A, Uhlmann M, Sekimoto A, Kawahara G (2010) Reynolds number dependence of mean flow structure in square duct turbulence. J Fluid Mech 644:107
34. Uhlmann M, Pinelli A, Kawahara G, Sekimoto A (2007) Marginally turbulent flow in a square duct. J Fluid Mech 588:153
35. Jiménez J, Moin P (1991) The minimal flow unit in near-wall turbulence. J Fluid Mech 225:213
36. Krasnov D, Zikanov O, Boeck T (2012) Numerical study of magnetohydrodynamic duct flow at high reynolds and hartmann numbers. J Fluid Mech 704:421
37. Flores O, Jiménez J (2010) Hierarchy of minimal flow units in the logarithmic layer. Phys Fluids 22:071704
38. Hoyas S, Jiménez J (2006) Scaling of the velocity fluctuations in turbulent channels up to $Re_\tau = 2003$. Phys Fluids 18:011702
39. del Álamo JC, Jiménez J (2003) Spectra of the very large anisotropic scales in turbulent channels. Phys Fluids 15:41
40. Ohlsson J, Schlatter P, Fischer PF, Henningson D (2010) Direct numerical simulation of separated flow in a three-dimensional diffuser. J Fluid Mech 650:307
41. Gessner FB, Eppich HM, Lund EG (1993) Reynolds number effects on the near-wall structure of turbulent flow along a streamwise corner. In: So RMC, Speziale CG, Launder BE (eds) Near wall turbulent flows. Elsevier, Amsterdam, pp 965–975
42. Gessner FB, Jones JB (1965) On some aspects of fully-developed turbulent flow in rectangular channels. J Fluid Mech 23:689
43. Vinuesa R, Schlatter P, Nagib HM (2015) On minimum aspect ratio for duct flow facilities and the role of side walls in generating secondary flows. J Turbul 16:588
44. Chevalier M, Schlatter P, Lundbladh A, Henningson DS (2007) A pseudo-spectral solver for incompressible boundary layer flows. Tech. Rep. TRITA-MEK 2007:07, Royal Institute of Technology, Stockholm, Sweden
45. Fischer P.F., Lottes J.W., Kerkemeier S.G. (2008) Nek5000: Open source spectral element CFD solver. http://nek5000.mcs.anl.gov
46. Patera AT (1984) A spectral element method for fluid dynamics: laminar flow in a channel expansion. J Comput Phys 54:468
47. Maday Y, Patera AT (1989) Spectral element methods for the Navier–Stokes equations. In: Noor AK (ed) State of the art surveys in computational mechanics. ASME, New York, pp 71–143
48. Guala M, Hommema SE, Adrian RJ (2006) Large-scale and very-large-scale motions in turbulent pipe flow. J Fluid Mech 554:521
49. Jiménez J, Hoyas S (2010) Turbulent fluctuations above the buffer layer of wall-bounded flows. J Fluid Mech 611:215
50. Chin C, Ooi ASH, Marusic I, Blackburn M (2010) The influence of pipe length on turbulence statistics computed from direct numerical simulation data. Phys Fluids 22:115107
51. Panton RL (1996) Incompressible flow, 2nd edn. Wiley, Colorado
52. Hunt JCR, Wray AA, Moin P (1998) Eddies, streams, and convergence zones in turbulent flows. Center for Turbulence Research (CTR) Proceedings of Summer Program
53. Chong MS, Perry AE, Cantwell BJ (1990) A general classification of three-dimensional flow fields. Phys Fluids 5:765
54. Zhou J, Adrian RJ, Balachandar S, Kendali TM (1990) Mechanisms for generating coherent packets of hairpin vortices. J Fluid Mech 387:353
55. Kida S, Miura H (1998) Identification and analysis of vortical structures. Eur J Mech B Fluids 17:471
56. Prandtl L (1926) Über die ausgebildete Turbulenz [turbulent flow]. Verh. 2nd Intl Kong. NACA Tech. Memo 62, 2nd Intl Kong. für Tech. Mech., Zürich. p. 435